

Experimental Investigation of Variations in Polycrystalline Hf_{0.5}Zr_{0.5}O₂ (HZO)-based MFIM

Tae Ryong Kim, Revanth Koduru, Zehao Lin, Graduate Student Member, *IEEE*, Peide. D. Ye, Fellow, *IEEE*, and Sumeet Kumar Gupta, Senior Member, *IEEE*

Abstract—Device-to-device variations in ferroelectric (FE) hafnium oxide-based devices pose a crucial challenge that limits the otherwise promising capabilities of this technology. Earlier simulation-based studies have identified polarization (P) domain nucleation and polycrystallinity as key contributors to these variations. In this work, we experimentally investigate the effect of these two factors on remanent polarization (P_R) variation in Hf_{0.5}Zr_{0.5}O₂ (HZO) based metal-ferroelectric-insulator-metal (MFIM) capacitors for different set voltages (V_{SET}) and FE thicknesses (T_{FE}). Our measurements reveal a non-monotonic behavior of P_R variations with V_{SET} , which is consistent with previous simulation-based predictions. For low and high- V_{SET} regions, we find that P_R variations are dictated primarily by saturation polarization (P_s) variations and are associated with the polycrystallinity in HZO. Our measurements also reveal that P_R variations peak near the coercive voltage (V_C), defined as the mid- V_{SET} region. We attribute the increase of P_R variation around V_C to the random nature and sharp P switching associated with domain nucleation, which is dominant near V_C . Further, we observe a reduction in the peak P_R variation as HZO thickness (T_{FE}) is scaled. We validate our arguments by establishing the correlation between the measured values of P_R with V_C and P_s . Our results display that a strong correlation exists between P_R and V_C in the mid- V_{SET} region and between P_R and P_s in the low and high- V_{SET} regions across various T_{FE} .

Index Terms— ferroelectric, HZO, device-to-device variation, domain nucleation, polycrystallinity, set voltage, FE layer thickness

I. INTRODUCTION

FERROELECTRIC (FE) materials are considered promising candidates for next-generation electronics due to their spontaneous non-zero polarization (P) and other unique characteristics [1], [2], [3], [4]. The discovery of

ferroelectricity in doped hafnium oxide (HfO₂) has triggered immense attraction due to its CMOS compatibility [5], [6]. This has led to the integration of HfO₂ in various devices, such as ferroelectric RAM (FERAM) [7], [8], ferroelectric field effect transistors (FEFETs) [6], [9], and ferroelectric tunnel junctions (FTJs) [10], [11] and their use in a range of applications [1], [2], [3], [4]. Among various dopants for HfO₂ (Si [12], Al [13], Y [14], La [15], etc.) [16], Zirconium (Zr) stands out for its lower annealing temperature (400-500°C) to exhibit FE properties [17], [18]. A low thermal budget facilitates the integration of Zr-doped HfO₂ (Hf_{1-x}Zr_xO₂ or HZO) with front-end-of-line (FEOL) conventional CMOS devices without introducing additional stress [18].

Despite their potential, several challenges hinder the commercialization of FE HZO devices [19], [20], [21], [22], [23], [24], [25]. Among those, device-to-device variations in device characteristics significantly impact the performance of HZO-based systems [21], [22], [23], [24], [25], [26]. Specifically, in the context of multi-state storage (multiple intermediate polarizations) [27], [28], where the state of FE-based devices is determined by applied V_{SET} (or V_{RESET}), device-to-device variations are shown to be significantly dependent on V_{SET} (or V_{RESET}) [24], [25]. For example, the read current [24] and threshold voltage [25] of FEFET, determined by the remanent polarization (P_R) of the FE layer in the gate stack, has been experimentally shown to display non-monotonic dependence on V_{SET} (V_{RESET}).

Several factors have been suggested as causes of P switching variations in HZO-based metal-ferroelectric-insulator-metal (MFIM), including polycrystallinity [29], [30], [31] multi-domain (MD) P switching [32], [33], [34], and the charge trap effects at the ferroelectric-insulator interface [35], [36]. Multiple simulation-based studies have highlighted the role of polycrystallinity and MD P switching in governing the trends in the variations of coercive voltage (V_C) and remanent polarization (P_R) from the standpoint of HZO-based MFIM capacitors [33], [34]. The variations in P switching characteristics in polycrystalline HZO devices are attributed to the dependence of P_R and V_C on the crystal orientation angle (θ) of the grains [33] and the phase distributions. Multi-domain (MD) P switching, prevalent in HZO due to its low gradient energy [32], is another crucial factor dictating variations due to its random nature (especially domain nucleation) [34]. Based on the phase-field simulations, the works in [33], [34], [37] have shown that P switching mechanisms – domain nucleation and domain growth – and domain characteristics are T_{FE} and V_{SET} -dependent, which causes P_R variation to depend on V_{SET}

This work was supported by NSF under grant number 2008412 and SRC under the Center for the Co-Design of Cognitive Systems (COCOSYS), one of the seven centers in JUMP 2.0, funded by SRC and DARPA.

Tae Ryong Kim, Revanth Koduru, and Sumeet Kumar Gupta are with the Elmore Family School of Electrical and Computer Engineering, Purdue University, West Lafayette, IN 47907 USA (e-mail: kim3804@purdue.edu; kodurur@purdue.edu; guptask@purdue.edu).

Zehao Lin and Peide. D. Ye are the Elmore Family School of Electrical and Computer Engineering and Birck Nanotechnology Center, Purdue University, West Lafayette, IN 47907 USA. (e-mail: lin1174@purdue.edu; yep@purdue.edu).

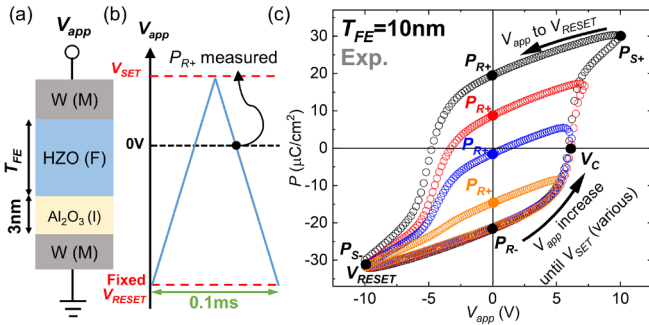


Fig. 1. (a) The schematic of the fabricated HZO-based metal-ferroelectric-insulator-metal (MFIM) capacitor (b) the waveform of 10kHz applied voltage (V_{app}) with positive remanent polarization (P_{R+}) measurement point and (c) measured polarization-voltage (P - V_{app}) curves averaged over 50 MFIM capacitors with 10nm of ferroelectric layer thickness (T_{FE}) for different set voltage (V_{SET})

and T_{FE} strongly. Despite these insights from simulations, experimental validation of these trends, especially with respect to T_{FE} , is still lacking. Moreover, exploring the correlation of variations with factors (like domain nucleation and polycrystallinity) is crucial to advancing the understanding of device-to-device variations in HZO devices.

This work experimentally characterizes the variations in P_R as a function of V_{SET} and T_{FE} and provides evidence that aligns with previous simulation-based analyses and insights. By measuring P_R from polarization-voltage (P - V) characteristics across 50 MFIM capacitors each for three different T_{FE} , we capture the relation between P_R , V_{SET} and T_{FE} . The key contributions of this work are summarized below.

- We experimentally establish that the standard deviation of P_R ($\sigma(P_R)$) exhibits a non-monotonic trend with respect to V_{SET} , peaking at V_{SET} near V_C .
- Our measurement results reveal that the peak value of $\sigma(P_R)$ reduces as T_{FE} is scaled.
- We support our experimental findings with the interpretations from our in-house 3D phase-field model.
- By plotting the correlation between the measured values of P_R , V_C , and P_S across different V_{SET} and T_{FE} , we establish the role of polycrystallinity/domain nucleation in dictating the P_R variations.

II. MFIM FABRICATION AND MEASUREMENTS

We fabricate HZO-based MFIM capacitors comprising 70nm tungsten (W) for the top and bottom metal electrodes, a ferroelectric HZO layer with various thicknesses ($T_{FE}=5, 7, 10$ nm), and a 3nm Al_2O_3 insulator or dielectric (DE) layer, as shown in Fig. 1(a). First, the W bottom electrode is deposited on a bare Si wafer using sputtering. Atomic layer deposition (ALD) is then utilized to deposit HZO and Al_2O_3 layers at 200°C. Following this, W is sputtered to form the top electrode. This is followed by 30s of rapid thermal annealing (RTA) at 300°C in the nitrogen (N_2) atmosphere. The capacitor area is defined by the top electrode, patterned as a circle with a 25 μ m radius through the lift-off process using photolithography.

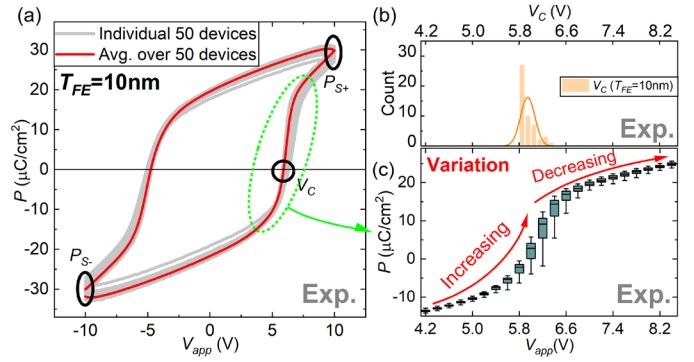


Fig. 2. (a) P - V_{app} of the major loop for 50 devices (grey: individual curves, red: averaged) (b) measured V_C distribution of 50 MFIM with $T_{FE}=10$ nm and (c) box plot depicting the P variation around V_C

The P - V measurements of 50 fabricated MFIM capacitors at each T_{FE} are performed using a Radiant Premier II Ferroelectric Tester through a probe station. The applied voltage (V_{app}) is swept at 10kHz frequency from a fixed V_{RESET} to a different V_{SET} (Fig. 1(b)). For consistency, V_{RESET} for each T_{FE} is selected to obtain a similar magnitude of average electric field (E -field) across the FE layer at V_{RESET} ($=-10, -8.3$ and -7.1 V for $T_{FE}=10, 7$ and 5 nm). (Note: the E -field is estimated using phase-field simulations). To minimize the effect of cycle-to-cycle variations [33], the P - V curves used in the analysis are averaged over five measurement cycles. Fig. 1(c) illustrates the P - V plots averaged for the 50 MFIM capacitors with $T_{FE}=10$ nm for various V_{SET} . All these curves start from negative saturation polarization (P_{S-}) at the fixed V_{RESET} , pass negative remanent polarization (P_{R-}) at $V_{app}=0$ V, and reach varying P values depending on V_{SET} . After that, P returns to P_{S-} at V_{RESET} as V_{app} is swept backward from V_{SET} . The P - V curves reach positive saturation polarization (P_{S+}) only for the major loop, where $|V_{SET}|=|V_{RESET}|$. The P_{R+} is measured at $V_{app}=0$ V on the return path from V_{SET} to V_{RESET} for each cycle. V_C is extracted as the voltage where $P=0$ on the path from V_{RESET} to V_{SET} in the major loop. Note that we consider the scenario where different V_{SET} values are applied to achieve multiple states of the MFIM from an initial fixed reset state (spontaneous state after the application of fixed V_{RESET}). Therefore, we characterize the standard deviation of P_{R+} ($\sigma(P_{R+})$) to analyze the device-to-device variation in remanent polarization. Due to the symmetry of P - V characteristics, analyzing P_{R-} for different V_{RESET} (after the application of fixed V_{SET} application) is equivalent to our analysis.

III. EXPERIMENTAL RESULTS

A. The Non-monotonic Trend of P_{R+} variation with V_{SET}

Let us begin by analyzing the dependence of P_{R+} variation on V_{SET} . From the measured P - V major loops from 50 MFIM capacitors with $T_{FE}=10$ nm, we can observe that device-to-device P variation is dependent on V_{app} (Fig. 2(a)). Notably, the P variation is maximized around V_C . A box plot of P zoomed around V_C along the forward path (i.e., as V_{app} increases from V_{RESET} to V_{SET}) illustrates this trend clearly (fig. 2(b) and (c)). The distribution of P broadens as V_{app} approaches the V_C range and narrows as V_{app} increases beyond V_C .

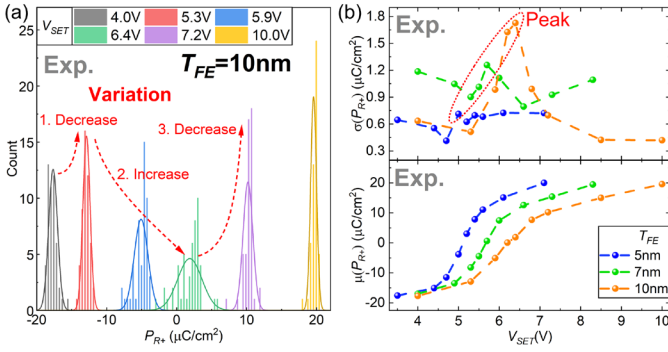


Fig. 3. (a) Measured P_{R+} distribution for 50 MFIM capacitors with $T_{FE}=10\text{nm}$ at different V_{SET} and (b) standard deviation (σ) and mean (μ) versus V_{SET} for different T_{FE} .

Due to this dependence of P variation on V_{app} , P_{R+} variation shows significant dependence on V_{SET} . A plot of the P_{R+} distribution for 50 MFIM capacitors with $T_{FE}=10\text{nm}$ at various V_{SET} values (Fig. 3(a)) reveals a significant dependence of P_{R+} variation on V_{SET} (Fig. 3(b)). $\sigma(P_{R+})$ shows a non-monotonic behavior with respect to V_{SET} (as also predicted via simulations in [30]). Initially, the distribution shows a mild reduction in $\sigma(P_{R+})$ as V_{SET} increases from 4.0V to 5.3V (region-1 or low- V_{SET} range). Following this, the distribution substantially increases its spread as V_{SET} increases from 5.3V to 6.2V (region-2 or mid- V_{SET} range). As V_{SET} increases further, $\sigma(P_{R+})$ reduces (region-3 or high- V_{SET} range). It can be observed, as shown in Fig. 2(b), that $\sigma(P_{R+})$ exhibits a peak at a particular V_{SET} , which is annotated as V_{peak} . Given that the mean P_{R+} ($\mu(P_{R+})$) at V_{peak} is close to 0 (Fig. 2(c)), it follows that $\sigma(P_{R+})$ reaches a peak point around $V_{SET} \sim V_C$. As T_{FE} decreases, we observe that the non-monotonicity is not as well-defined as for $T_{FE} = 10\text{nm}$ and the peak $\sigma(P_{R+})$ reduces. Let us discuss this T_{FE} -dependence in more detail next.

B. The Effect of T_{FE} on Device-to-Device Variations

The first key impact of T_{FE} is observed in the mid- V_{SET} range near V_C (Fig. 3(b)). As T_{FE} scales down, the peak variations show a significant decrease (as also predicted in the former simulation-based works [34]). From $1.73\mu\text{m}^2/\text{cm}^2$ at $T_{FE}=10\text{nm}$, the peak value of $\sigma(P_{R+})$ reduces to $1.11\mu\text{m}^2/\text{cm}^2$ ($0.73\times$) at $T_{FE}=7\text{nm}$ and $0.71\mu\text{m}^2/\text{cm}^2$ ($0.41\times$) at $T_{FE}=5\text{nm}$. The simulations in [34] attribute the decrease in peak $\sigma(P_{R+})$ to reduced V_C variation with T_{FE} scaling. We confirm this experimentally by measuring the V_C variations for various T_{FE} . From the measurements, the V_C distributions display reduced variation as T_{FE} decreases (Fig. 4(b)). Compared to $T_{FE}=10\text{nm}$, $\sigma(V_C)$ reduces to $0.72\times$ at $T_{FE}=7\text{nm}$ and $0.28\times$ at $T_{FE}=5\text{nm}$. Therefore, we can verify through experiment that a decrease in the peak $\sigma(P_{R+})$ largely correlates with lower V_C variation at a scaled T_{FE} . Also, the V_C distributions explain the V_{peak} shift towards lower V_{SET} . The mean value of V_C ($\mu(V_C)$) shows a shift to a lower value as T_{FE} is scaled ($6.0\text{V} \rightarrow 5.5\text{V} \rightarrow 5.1\text{V}$ for $T_{FE}=10, 7,$ and 5nm). This is attributed to increased E -field for lower T_{FE} at a given V_{app} . This more or less aligns with V_{peak} shifts shown in Fig. 2(b) ($6.4\text{V} \rightarrow 5.7\text{V} \rightarrow 5.0\text{V}$ for $T_{FE}=10, 7,$ and 5nm). Therefore, from our experimental findings, we verify that V_{peak} is around V_C across different T_{FE} and reduces as T_{FE} decreases.

Now, we turn our attention to the low and high- V_{SET} range. Instead of displaying a monotonic trend with T_{FE} as predicted in

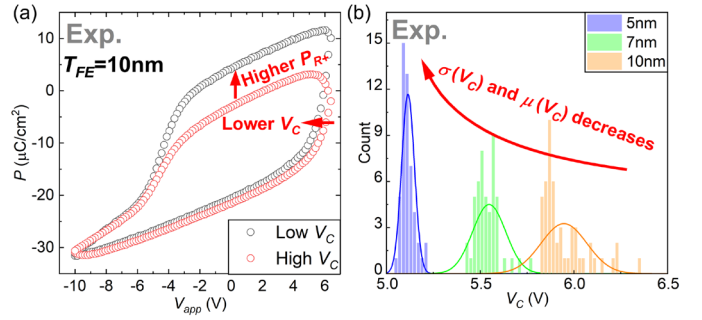


Fig. 4. (a) P - V minor loops ($V_{SET}=6.4\text{V}$) with different V_C . At V_{SET} range around V_C (region-2 in Fig. 3(a)), P_{R+} is largely dependent on V_C (b) measured V_C distribution from 50 MFIM capacitors of different T_{FE} .

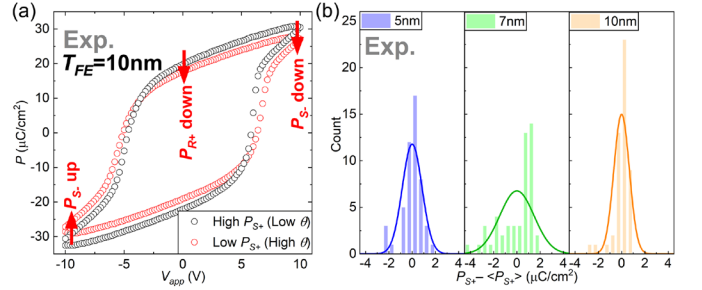


Fig. 5. (a) P - V major loops ($V_{SET}=10.0\text{V}$) with different P_{S+} . At high- V_{SET} range, P_{R+} is largely dependent on P_{S+} (b) distribution of $P_{S+} - \langle P_{S+} \rangle$ from 50 devices of different T_{FE} . The $\sigma(P_{S+})$ trends in Fig. 3(b) at the low (region-1) and high- V_{SET} range (region-3) follow that of the P_{S+} distribution. $\langle \rangle$ indicates an average value.

previous simulation-based works [34], $\sigma(P_{R+})$ is the highest for $T_{FE}=7\text{nm}$, followed by 5nm and 10nm for both low and high- V_{SET} regions. In the high- V_{SET} region (especially for the major P - V loop), P_{S+} determines P_{R+} because the P domains rarely switch during the backward sweep of V_{app} from V_{SET} (where $P=P_{S+}$) to 0V (where $P=P_{R+}$) where a dielectric response is prevailing [34]. As can be observed in Fig. 4(a), the MFIM sample with lower P_{S+} exhibits lower P_{R+} , which suggests that variation in P_{R+} is dictated by P_{S+} variation in the high- V_{SET} range. From the measurements, P_{S+} distributions exhibit the maximum variation for $T_{FE}=7\text{nm}$ followed by 5nm and 10nm (Fig. 5(b)), which have the same trend as the P_{R+} variation at the high- V_{SET} region.

In the low- V_{SET} region, two key factors come into the picture. First, the dielectric response is a significant component, especially in the region where V_{app} is swept from V_{RESET} (where $P=P_{S-}$) to V_{SET} and from V_{SET} to 0V (where $P=P_{R+}$). In particular, lower (more negative) P_{S-} leads to lower P_{R+} . Thus, the variation in P_{S-} directly leads to P_{R+} variation. Second, since $P_{S-} (<0)$ and $P_{S+} (>0)$ are more or less symmetric (i.e., more negative P_{S-} implies higher P_{S+}) as shown in Fig. 5(a), a strong negative correlation exists between P_{S-} and P_{S+} . These two factors lead to a correlation between P_{S+} and P_{R+} – i.e., a larger value of P_{S+} is associated with a smaller value of P_{R+} . Due to this, P_{R+} variation is mainly dictated by P_{S+} variation in the low- V_{SET} region. However, it is notable that the correlation direction between P_{R+} and P_{S+} is opposite in low and high- V_{SET} regions, which will be described in more detail later.

IV. ANALYSIS USING 3D PHASE-FIELD SIMULATION

A. 3D Multi-grain Phase-Field Simulation Framework

To gain further insights into the mechanisms governing the

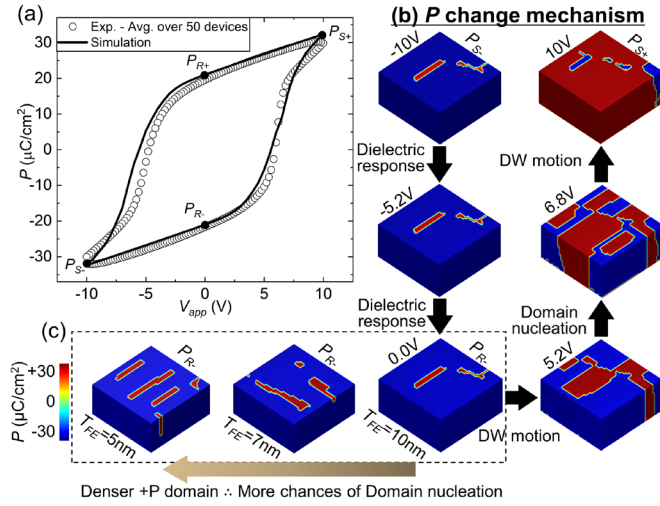


Fig. 6. (a) Simulated and experimental P - V with $T_{FE}=10\text{nm}$. The experimental P - V is averaged over 50 MFIM devices (b) P maps from the phase-field simulation illustrating the P changing mechanism as V_{app} increases from -10V (V_{RESET}) to 10V (V_{SET}) and (c) simulated P maps of P_{R-} for different T_{FE} ($=5, 7,$ and 10nm)

P_{R+} variations, we utilize a calibrated 3D phase-field model [33], [34] to simulate the MFIM structure. Our 3D multi-grain phase-field framework calculates the P profile in an MFIM stack by solving time-dependent Ginzburg Landau (TDGL) and Poisson's equations. The model captures the effect of the polycrystalline nature of HZO by associating the 3D grain-growth model with the grain orientation angle (θ) – the angle of P direction within the grain with respect to physical out-of-plane direction (details in [33], [34]). The black solid line in Fig. 6(a) represents the calibrated P - V curve from the model for $T_{FE}=10\text{nm}$, which closely matches the average of measured P - V curves over 50 devices (black symbols). The P profiles from the phase-field simulation (Fig. 6(b)) with increasing V_{app} illustrate the voltage dependence of P switching mechanisms in the FE layer. As V_{app} increases from V_{RESET} ($=-10\text{V}$), HZO initially exhibits dielectric response starting from P_{S-} , followed by domain wall (DW) motion or domain growth. Afterward, domain nucleation occurs around V_C , followed by DW motion until HZO reaches P_{S+} at V_{SET} ($=10\text{V}$).

B. The Effect of Domain Nucleation on P_{R+} Variation

The strong influence of domain nucleation around V_C (mid- V_{SET} range) leads to large variations in P_{R+} . The increase in $\sigma(P_{R+})$ around V_C stems from the inherent randomness of domain nucleation and the associated sharp P switching [34]. The randomness in the polycrystalline structure of HZO and P domain configurations leads to the random nature of domain nucleation. As a result, different samples nucleate at different V_{app} . Further, domain nucleation is associated with sharp P switching (a large amount of P switched in a small voltage range) compared to DW motion. As a result, when a subset of samples nucleates at lower V_{app} (early nucleating samples), it switches to a higher P , widening the distribution of P and that of P_{R+} in turn. This widening is reduced after V_{SET} surpasses the nucleation range, where domain nucleation across all the devices is complete.

The reduction in peak $\sigma(P_{R+})$ with T_{FE} scaling can also be attributed to multi-domain (MD) P switching. In a thinner FE

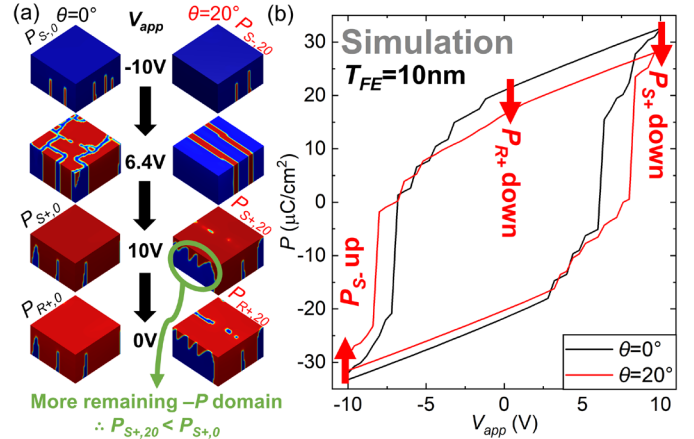


Fig. 7. (a) P maps during the V_{app} sweep (-10V (V_{RESET}) $\rightarrow 10\text{V}$ (V_{SET}) $\rightarrow 0\text{V}$) and (b) P - V loops of HZO samples with $\theta=0^\circ$ and 20° from the phase-field simulations

layer, the P_{R-} domain patterns become denser (Fig. 6(c)) to compensate for increasing depolarization energy [37]. This increased domain density limits the room for domain nucleation and thus suppresses it. Since DW motion exhibits a lower degree of randomness than domain nucleation, the randomness in P switching decreases. This decrease in randomness can also be observed from the measured V_C distributions for different T_{FE} in Fig. 4(b), as noted before. At higher T_{FE} , the increased likelihood of domain nucleation results in different samples switching at different V_{app} , leading to higher V_C variations.

C. The Effect of Polycrystallinity on P_{R+} Variation

Let us now focus on the low and high- V_{SET} range. We find that the $\sigma(P_{R+})$ follows the trend of $\sigma(P_{S+})$ in Sec III. B. Therefore, the main factor for the P_{S+} variation needs to be identified to understand the reason for P_{R+} in these regions.

For this, polycrystallinity in HZO offers an explanation. In polycrystalline HZO, which consists of multiple grains with various θ , primarily the E -field component parallel to the P direction (out-of-plane) contributes to the P switching [33]. Therefore, at MFIM with higher θ , a stronger E -field is required to switch $-P$ domains to $+P$ domains. Consequently, grains with larger θ have more $-P$ domains as V_{app} is swept from V_{RESET} to V_{SET} [33]. Our phase-field model captures this phenomenon, as shown in Fig. 7(a). At $V_{app}=10\text{V}$, more $-P$ domains are observed in the grain with $\theta=20^\circ$. These remaining $-P$ domains at 10V lead to lower P_{S+} , as shown in P - V_{app} from the phase-field model (Fig. 7(b)). Since the dielectric response is prevalent during the backward V_{app} sweep from 10V to 0V (Fig. 7(a)), lower P_{S+} directly leads to lower P_{R+} , which is also captured by P - V_{app} in Fig. 7(b). These results show that in the high- V_{SET} range, polycrystallinity-induced P_{S+} variation leads to P_{R+} variation. Likewise, in the low- V_{SET} range, where a dielectric response is a primary P change mechanism during the V_{app} sweep (as noted before), polycrystallinity-induced P_{S-} variation leads to P_{R+} variation.

It may be noted that interface trap density variation causes P variation in the mid and high- V_{SET} since it has been shown the trap effects primarily appear at $V_{app}>V_C$ [36]. Therefore, if the trap effect is significant, P_{R+} variation trends in the high- V_{SET} region should be different from the low- V_{SET} region (where the

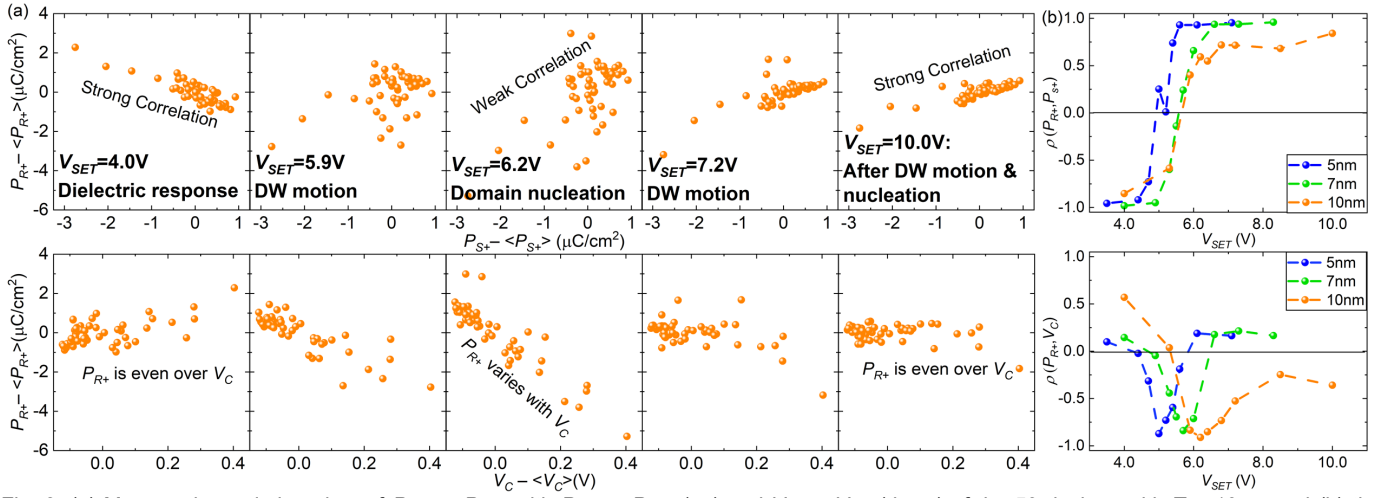


Fig. 8. (a) Measured correlation plots of $P_{R+} - \langle P_{R+} \rangle$ with $P_{S+} - \langle P_{S+} \rangle$ (up) and $V_C - \langle V_C \rangle$ (down) of the 50 devices with $T_{FE}=10\text{nm}$ and (b) the correlation coefficient of P_{R+} with P_{S+} ($\rho(P_{S+}, P_{R+})$) (up) and with V_C ($\rho(V_C, P_{R+})$) (down) as a function of V_{SET} for different T_{FE} . At the low and high V_{SET} (4.0 and 10.0V), the effect of polycrystallinity is stronger, while domain nucleation has a huge effect at the middle V_{SET} (6.2V).

charge trap effect is negligible). However, in our experimental result, $\sigma(P_{R+})$ displays the same trend in the low and high- V_{SET} regions, which suggests a key role of polycrystallinity and MD effects in dictating variations, which we analyze in this work.

The dependence of P_{S+} variation with T_{FE} requires further investigation as P_{S+} variation does not exhibit an explicit trend with respect to T_{FE} in the experimental results. We speculate that T_{FE} -dependent factors, not captured in our phase-field model, such as charge trapping at the FE-DE interface [35], [36], non-uniform strain [38] and the effect of grain size on phase distribution [39] also play a role in the P_{S+} variation of MFIM capacitors, besides HZO polycrystallinity.

V. EXPERIMENTAL ANALYSIS OF THE CORRELATIONS

We will now examine the correlation between the measured P_{R+} , V_C , and P_{S+} values for individual devices. By analyzing these correlations, we aim to highlight the role of MD P switching and polycrystallinity in influencing the variations across different V_{SET} values.

Fig. 8(a) displays scatter plots showing the correlation of P_{R+} with P_{S+} and V_C for different V_{SET} values for 50 MFIM devices with $T_{FE}=10\text{nm}$. Initially, at low V_{SET} , P_{R+} shows a strong correlation with P_{S+} , which implies a considerable influence of polycrystallinity. As V_{SET} approaches mid- V_{SET} range values (close to V_C), the correlation of P_{R+} with P_{S+} becomes more dispersed, with the maximum dispersion at $V_{SET}=6.2\text{V}$. At this voltage (i.e., as V_{SET} approaches V_C), the influence of polycrystallinity on P_{R+} variations is diminished. However, as V_{SET} increases further and reaches 10V, the effect of polycrystallinity appears again, showing a strong correlation between P_{R+} and P_{S+} . Notably, P_{R+} negatively correlates with P_{S+} at the low- V_{SET} range (4.0V) while positively at the high- V_{SET} range (10.0V). At high- V_{SET} , MFIM with higher P_{S+} yields higher P_{R+} , as discussed in Section III. B, which leads to a positive correlation. On the other hand, at the low- V_{SET} range, P_{R+} is mainly determined by P_{S-} —i.e., higher P_{S-} (less negative P_{S-}) yields higher P_{R+} . Moreover, recalling the symmetry between P_{S-} and P_{S+} , a higher P_{S-} implies a lower P_{S+} . Combining these two correlations, we can deduce that lower P_{S+} results in higher P_{R+} in the low- V_{SET} range. This results in a

negative correlation at $V_{SET}=4.0\text{V}$.

Now, let us focus on the correlation of P_{R+} with V_C . At low V_{SET} values ($V_{SET}=4.0\text{V}$), P_{R+} shows minimal correlation with V_C . Regardless of V_C , the data points display a relatively even distribution representing less effect of V_C on P_{R+} . As V_{SET} increases, approaching 6.2V, the correlation turns into a strong negative correlation because capacitors with low V_C undergo higher P switching at a given V_{app} . With further increase in V_{SET} (high- V_{SET} range) where most domain nucleation is completed, MD P switching has less contribution to the P_{R+} variation, making the correlation between P_{R+} and V_C weaker.

The correlation coefficient (ρ) of P_{R+} with P_{S+} ($\rho(P_{R+}, P_{S+})$) and V_C ($\rho(P_{R+}, V_C)$) across different V_{SET} values (shown in Fig. 6(b)) summarize the discussion above. Initially, $\rho(P_{R+}, P_{S+})$ is around -1, indicating a strong negative correlation. It approaches 0 at $V_{SET} \sim V_C$ and reaches +1 at the high V_{SET} values. For $\rho(P_{R+}, V_C)$, the coefficient dips down to almost -1 around V_C , representing a substantial negative correlation, and remains closer to 0 at other V_{SET} values. This trend is consistent across all T_{FE} values (5nm, 7nm and 10nm), suggesting that polycrystallinity primarily dictates P_{R+} variations at low and high- V_{SET} values, whereas MD switching (especially domain nucleation) is a dominant factor in the mid- V_{SET} range.

VI. CONCLUSION

We experimentally investigated P_R variations in HZO-based MFIM capacitors and their dependence on V_{SET} and T_{FE} . Our results confirm the non-monotonic trend of $\sigma(P_{R+})$ as a function of V_{SET} , consistent with previous simulation-based work. In the mid- V_{SET} region, the effect of MD P switching becomes apparent, showing a peak in P_R variation. The random nature and sharp P switching increase the spatial P variation. This effect diminishes as FE layer thickness decreases due to suppressed domain nucleation. On the other hand, at low and high- V_{SET} , polycrystallinity of HZO becomes dominant over MD P switching. By analyzing the correlation between measured P_R , V_C and P_S across different V_{SET} , we highlight which factor has more effect on P_R variation. In the mid- V_{SET} region, P_R exhibits a strong (weak) correlation with V_C (P_S),

suggesting the primary role of MD switching. In both the low- and high- V_{SET} regions, a strong (weak) correlation with $P_S(V_C)$ is observed, which points to the significance of polycrystallinity-induced variations.

REFERENCES

- [1] Y. Xu, *Ferroelectric Materials and Their Applications*. Elsevier, 2013.
- [2] K. Uchino, *Ferroelectric Devices*. CRC Press, 2018.
- [3] N. Setter et al., “Ferroelectric thin films: Review of materials, properties, and applications,” *Journal of Applied Physics*, vol. 100, no. 5, p. 051606, Sep. 2006, doi: 10.1063/1.2336999.
- [4] L. W. Martin and A. M. Rappe, “Thin-film ferroelectric materials and their applications,” *Nat Rev Mater*, vol. 2, no. 2, pp. 1–14, Nov. 2016, doi: 10.1038/natrevmats.2016.87.
- [5] T. S. Böschke, J. Müller, D. Bräuhäus, U. Schröder, and U. Böttger, “Ferroelectricity in hafnium oxide thin films,” *Applied Physics Letters*, vol. 99, no. 10, p. 102903, Sep. 2011, doi: 10.1063/1.3634052.
- [6] S. Dünkel et al., “A FeFET based super-low-power ultra-fast embedded NVM technology for 22nm FDSOI and beyond,” in *2017 IEEE International Electron Devices Meeting (IEDM)*, Dec. 2017, p. 19.7.1-19.7.4. doi: 10.1109/IEDM.2017.8268425.
- [7] T. Francois et al., “Demonstration of BEOL-compatible ferroelectric Hf_{0.5}Zr_{0.5}O₂ scaled FeRAM co-integrated with 130nm CMOS for embedded NVM applications,” in *2019 IEEE International Electron Devices Meeting (IEDM)*, Dec. 2019, p. 15.7.1-15.7.4. doi: 10.1109/IEDM19573.2019.8993485.
- [8] J. Okuno et al., “SoC Compatible 1T1C FeRAM Memory Array Based on Ferroelectric Hf_{0.5}Zr_{0.5}O₂,” in *2020 IEEE Symposium on VLSI Technology*, Jun. 2020, pp. 1–2. doi: 10.1109/VLSITechnology18217.2020.9265063.
- [9] K. Ni et al., “Critical Role of Interlayer in Hf_{0.5}Zr_{0.5}O₂ Ferroelectric FET Nonvolatile Memory Performance,” *IEEE Transactions on Electron Devices*, vol. 65, no. 6, pp. 2461–2469, Jun. 2018, doi: 10.1109/TED.2018.2829122.
- [10] Y. Goh and S. Jeon, “The effect of the bottom electrode on ferroelectric tunnel junctions based on CMOS-compatible HfO₂,” *Nanotechnology*, vol. 29, no. 33, p. 335201, Aug. 2018, doi: 10.1088/1361-6528/aac6b3.
- [11] H. Ryu, H. Wu, F. Rao, and W. Zhu, “Ferroelectric Tunneling Junctions Based on Aluminum Oxide/Zirconium-Doped Hafnium Oxide for Neuromorphic Computing,” *Sci Rep*, vol. 9, p. 20383, Dec. 2019, doi: 10.1038/s41598-019-56816-x.
- [12] P. D. Lomenzo, Q. Takmeel, S. Moghaddam, and T. Nishida, “Annealing behavior of ferroelectric Si-doped HfO₂ thin films,” *Thin Solid Films*, vol. 615, pp. 139–144, Sep. 2016, doi: 10.1016/j.tsf.2016.07.009.
- [13] B. Ku, Y. Ma, H. Han, W. Xuan, and C. Choi, “Effects of etching process and annealing temperature on the ferroelectric properties of atomic layer deposited Al-doped HfO₂ thin film,” *Nanotechnology*, vol. 33, no. 42, p. 425205, Jul. 2022, doi: 10.1088/1361-6528/ac7cf7.
- [14] J. Müller et al., “Ferroelectricity in yttrium-doped hafnium oxide,” *Journal of Applied Physics*, vol. 110, no. 11, p. 114113, Dec. 2011, doi: 10.1063/1.3667205.
- [15] U. Schroeder et al., “Lanthanum-Doped Hafnium Oxide: A Robust Ferroelectric Material,” *Inorg. Chem.*, vol. 57, no. 5, pp. 2752–2765, Mar. 2018, doi: 10.1021/acs.inorgchem.7b03149.
- [16] R. Batra, T. D. Huan, G. A. Jr. Rossetti, and R. Ramprasad, “Dopants Promoting Ferroelectricity in Hafnia: Insights from a comprehensive Chemical Space Exploration,” *Chem. Mater.*, vol. 29, no. 21, pp. 9102–9109, Nov. 2017, doi: 10.1021/acs.chemmater.7b02835.
- [17] J. Müller et al., “Ferroelectricity in Simple Binary ZrO₂ and HfO₂,” *Nano Lett.*, vol. 12, no. 8, pp. 4318–4323, Aug. 2012, doi: 10.1021/nl302049k.
- [18] S. J. Kim et al., “Large ferroelectric polarization of TiN/Hf_{0.5}Zr_{0.5}O₂/TiN capacitors due to stress-induced crystallization at low thermal budget,” *Applied Physics Letters*, vol. 111, no. 24, p. 242901, Dec. 2017, doi: 10.1063/1.4995619.
- [19] N. Tasneem et al., “Trap Capture and Emission Dynamics in Ferroelectric Field-Effect Transistors and their Impact on Device Operation and Reliability,” in *2021 IEEE International Electron Devices Meeting (IEDM)*, Dec. 2021, p. 6.1.1-6.1.4. doi: 10.1109/IEDM19574.2021.9720615.
- [20] Z. Wang et al., “Depolarization Field Induced Instability of Polarization States in HfO₂ Based Ferroelectric FET,” in *2020 IEEE International Electron Devices Meeting (IEDM)*, Dec. 2020, p. 4.5.1-4.5.4. doi: 10.1109/IEDM13553.2020.9372098.
- [21] P. Sharma et al., “Impact of total and partial dipole switching on the switching slope of gate-last negative capacitance FETs with ferroelectric hafnium zirconium oxide gate stack,” in *2017 Symposium on VLSI Technology*, Jun. 2017, pp. T154–T155. doi: 10.23919/VLSIT.2017.7998160.
- [22] M. Pešić et al., “Variability sources and reliability of 3D — FeFETs,” in *2021 IEEE International Reliability Physics Symposium (IRPS)*, Mar. 2021, pp. 1–7. doi: 10.1109/IRPS46558.2021.9405118.
- [23] M. Pešić and B. Beltrando, “Embedding ferroelectric HfOx in memory hierarchy: Material- defects - device entanglement,” in *2021 IEEE International Electron Devices Meeting (IEDM)*, Dec. 2021, p. 33.4.1-33.4.4. doi: 10.1109/IEDM19574.2021.9720623.
- [24] K. Chatterjee et al., “Challenges to Partial Switching of Hf_{0.8}Zr_{0.2}O₂ Gated Ferroelectric FET for Multilevel/Analog or Low-Voltage Memory Operation,” *IEEE Electron Device Letters*, vol. 40, no. 9, pp. 1423–1426, Sep. 2019, doi: 10.1109/LED.2019.2931430.
- [25] T. Ali et al., “A Multilevel FeFET Memory Device based on Laminated HSO and HZO Ferroelectric Layers for High-Density Storage,” in *2019 IEEE International Electron Devices Meeting (IEDM)*, Dec. 2019, p. 28.7.1-28.7.4. doi: 10.1109/IEDM19573.2019.8993642.
- [26] K. Ni, W. Chakraborty, J. Smith, B. Grisafe, and S. Datta, “Fundamental Understanding and Control of Device-to-Device Variation in Deeply Scaled Ferroelectric FETs,” in *2019 Symposium on VLSI Technology*, Jun. 2019, pp. T40–T41. doi: 10.23919/VLSIT.2019.8776497.
- [27] M. Jerry et al., “A ferroelectric field effect transistor based synaptic weight cell,” *J. Phys. D: Appl. Phys.*, vol. 51, no. 43, p. 434001, Aug. 2018, doi: 10.1088/1361-6463/aad6f8.
- [28] S. Dutta et al., “Biologically Plausible Ferroelectric Quasi-Leaky Integrate and Fire Neuron,” in *2019 Symposium on VLSI Technology*, Jun. 2019, pp. T140–T141. doi: 10.23919/VLSIT.2019.8776487.
- [29] M. Hyuk Park et al., “Surface and grain boundary energy as the key enabler of ferroelectricity in nanoscale hafnia-zirconia: a comparison of model and experiment,” *Nanoscale*, vol. 9, no. 28, pp. 9973–9986, 2017, doi: 10.1039/C7NR02121F.
- [30] S. D. Hyun et al., “Dispersion in Ferroelectric Switching Performance of Polycrystalline Hf_{0.5}Zr_{0.5}O₂ Thin Films,” *ACS Appl. Mater. Interfaces*, vol. 10, no. 41, pp. 35374–35384, Oct. 2018, doi: 10.1021/acsami.8b13173.
- [31] C. Garg et al., “Impact of Random Spatial Fluctuation in Non-Uniform Crystalline Phases on the Device Variation of Ferroelectric FET,” *IEEE Electron Device Letters*, vol. 42, no. 8, pp. 1160–1163, Aug. 2021, doi: 10.1109/LED.2021.3087335.
- [32] T. K. Paul, A. K. Saha, and S. K. Gupta, “Direction-Dependent Lateral Domain Walls in Ferroelectric Hafnium Zirconium Oxide and their Gradient Energy Coefficients: A First-Principles Study,” *Advanced Electronic Materials*, vol. 10, no. 1, p. 2300400, 2024, doi: 10.1002/aelm.202300400.
- [33] R. Koduru, A. K. Saha, M. Si, X. Lyu, P. D. Ye, and S. K. Gupta, “Variation and Stochasticity in Polycrystalline HZO based MFIM: Grain-Growth Coupled 3D Phase Field Model based Analysis,” in *2021 IEEE International Electron Devices Meeting (IEDM)*, Dec. 2021, p. 15.2.1-15.2.4. doi: 10.1109/IEDM19574.2021.9720564.
- [34] R. Koduru, I. Ahmed, A. K. Saha, X. Lyu, P. Ye, and S. K. Gupta, “Phase-field simulations of polarization variations in polycrystalline Hf_{0.5}Zr_{0.5}O₂ based MFIM: Voltage dependence and dynamics,” *Journal of Applied Physics*, vol. 134, no. 8, p. 084104, Aug. 2023, doi: 10.1063/5.0158997.
- [35] M. Si, X. Lyu, and P. D. Ye, “Ferroelectric Polarization Switching of Hafnium Zirconium Oxide in a Ferroelectric/Dielectric Stack,” *ACS Appl. Electron. Mater.*, vol. 1, no. 5, pp. 745–751, May 2019, doi: 10.1021/acsaelm.9b00092.
- [36] J. Li, M. Si, Y. Qu, X. Lyu, and P. D. Ye, “Quantitative Characterization of Ferroelectric/Dielectric Interface Traps by Pulse Measurements,” *IEEE Transactions on Electron Devices*, vol. 68, no. 3, pp. 1214–1220, Mar. 2021, doi: 10.1109/TED.2021.3053497.
- [37] A. K. Saha, M. Si, K. Ni, S. Datta, P. D. Ye, and S. K. Gupta, “Ferroelectric Thickness Dependent Domain Interactions in FEFETs for Memory and Logic: A Phase-field Model based Analysis,” in *2020 IEEE International Electron Devices Meeting (IEDM)*, Dec. 2020, p. 4.3.1-4.3.4. doi: 10.1109/IEDM13553.2020.9372099.
- [38] M. Hyuk Park, H. Joon Kim, Y. Jin Kim, T. Moon, and C. Seong Hwang, “The effects of crystallographic orientation and strain of thin Hf_{0.5}Zr_{0.5}O₂ film on its ferroelectricity,” *Applied Physics Letters*, vol. 104, no. 7, p. 072901, Feb. 2014, doi: 10.1063/1.4866008.
- [39] C. Künneth, R. Materlik, and A. Kersch, “Modeling ferroelectric film properties and size effects from tetragonal interlayer in Hf_{1-x}Zr_xO₂ grains,” *Journal of Applied Physics*, vol. 121, no. 20, p. 205304, May 2017, doi: 10.1063/1.4983811.